

Anatomical, Blood Oxygenation Level-Dependent, and Blood Flow MRI of Nonhuman Primate (Baboon) Retina

Yi Zhang,^{1,2} Hsiao-Ying Wey,^{1,2} Oscar San Emeterio Nateras,^{1,2} Qi Peng,^{1,2} Bryan H. De La Garza,^{1,2} and Timothy Q. Duong^{1–5*}

The goal of this study was to demonstrate high-resolution anatomical, blood oxygenation level-dependent, and blood flow MRI on large nonhuman primate retinas using a 3-Tesla clinical scanner as a first step toward translation. Baboon was chosen because of its evolutionary similarity to human. Anesthetized preparation, free of eye-movement artifacts, was used to evaluate clinical scanner hardware feasibility and optimize multimodal protocols for retinal MRI. Anatomical MRI ($0.1 \times 0.2 \times 2.0 \text{ mm}^3$) before contrast-agent injection detected three alternating bright–dark–bright layers. The hyperintense inner strip nearest to the vitreous was enhanced by an intravascular contrast agent, which likely included the ganglion and bipolar cell layer and the embedded retinal vessels. The hypointense middle strip showed no contrast enhancement, which likely included the avascular outer nuclear layer and photoreceptor segments. The hyperintense outer strip showed contrast enhancement, which likely corresponded to the choroid vascular layer. In the posterior retina, the total thickness including the choroid was $617 \pm 101 \mu\text{m}$ (\pm standard deviation, $n = 7$). Blood oxygenation level-dependent functional MRI ($0.3 \times 0.6 \times 2.0 \text{ mm}^3$) of oxygen inhalation relative to air increased the signals by $6.5 \pm 1.4\%$. Basal blood flow ($2 \times 2 \times 2 \text{ mm}^3$) was $83 \pm 30 \text{ mL}/100 \text{ g}/\text{min}$ (air), and hypercapnia increased blood flow by $25 \pm 9\%$ ($P < 0.05$). This study demonstrates multimodal MRI to image anatomy, physiology, and function on large nonhuman primate retinas using a clinical scanner, offering encouraging data to explore human applications. Magn Reson Med 66:546–554, 2011. © 2011 Wiley-Liss, Inc.

Key words: high-resolution MRI; blood oxygenation level-dependent; blood flow; choroid; retinal diseases; high-resolution fMRI; hyperoxia; hypercapnia

The retina is composed of three highly structured cell layers: photoreceptor layer, bipolar/amacrine cell layer, and ganglion cell layer (GCL) (1). The adjacent nuclear cell layers are connected by synapses. Two separate blood supplies—the retinal and choroidal vasculatures (2)—nourish the retina. The retinal vasculature exists primarily within the GCL, but does project a deep planar capillary bed into the bipolar cell layer. The choroidal vasculature is located directly beneath the photoreceptor layer, sandwiched between the retinal pigment epithelium and the sclera. The photoreceptor layer is completely avascular. Choroid (CH) blood flow (BF) is many times higher than retinal BF, and they are regulated differently in responses to stimulations (2). Some retinal diseases, such as diabetic retinopathy, glaucoma, and macular degeneration, may have differential effects on different vascular and/or tissue layers in terms of anatomy, blood oxygenation, BF and their responses to stimulations (3,4). Thus, the ability to noninvasively image these clinically relevant parameters in vivo could have important applications.

Historically, the retina has been studied using optical imaging techniques. Fundus imaging, scanning laser ophthalmoscopy, and optical coherence tomography (5) are widely used to image retinal anatomy. Lifetime phosphorescent imaging (6) and spectral reflectance (7) are used for detecting vascular oxygenation changes. Fluorescein angiography (8), indocyanin-green angiography (9), laser Doppler flowmetry (10), and laser speckle imaging (11) are used to measure relative BF or blood velocity. Optical imaging methods have high temporal and spatial resolutions but require unobstructed light paths, are usually qualitative, and have small field of view (FOV). Eye diseases, such as senile cataract and vitreous hemorrhage, often preclude applications of optical retinal imaging techniques. With the exception of optical coherence tomography, which is predominantly used for anatomical imaging to date, optical imaging techniques have ambiguous depth resolution.

By contrast, magnetic resonance imaging (MRI) provides noninvasive high-resolution anatomical, physiological, and functional information without depth limitation, although the spatiotemporal resolution of MRI is lower compared with that of optics. Anatomical, blood oxygenation level-dependent (BOLD), and BF MRI has been widely used to image small brain substructures including columnar (12–14) and laminar (15,16) structures in the brains of humans and animal models. More recently, multimodal MRI has been applied to study the retinas of small anesthetized animals. These included

¹Research Imaging Institute, University of Texas Health Science Center, San Antonio, Texas, USA.

²Department of Radiology, University of Texas Health Science Center, San Antonio, Texas, USA.

³Department of Ophthalmology, University of Texas Health Science Center, San Antonio, Texas, USA.

⁴Department of Physiology, University of Texas Health Science Center, San Antonio, Texas, USA.

⁵South Texas Veterans Health Care System, San Antonio, Texas, USA.

Grant sponsor: NIH/NEI; Grant numbers: R01 EY014211, EY018855; Grant sponsor: Department of Veterans Affairs; Grant sponsor: Translational Technology Research Grant via the Clinical Translational Science Award (CTSA); Grant number: UL1RR025767; Grant sponsor: American Heart Association's Established Investigator Award; Grant number: EIA 0940104N.

*Correspondence to: Timothy Q. Duong, Ph.D., University of Texas Health Science Center at San Antonio, Research Imaging Institute, 8403 Floyd Curl Dr, San Antonio, Texas 78229. E-mail: duongt@uthscsa.edu

Received 26 October 2010; revised 4 December 2010; accepted 5 January 2011.

DOI 10.1002/mrm.22853

Published online 28 February 2011 in Wiley Online Library (wileyonlinelibrary.com).

© 2011 Wiley-Liss, Inc.

anatomical layer resolution of the rat and cat retinas (17,18), relaxation and diffusion time constants of different layers of the rat and mouse retinas (18), BOLD functional MRI (fMRI) of physiological (17) and visual (19) stimulations of the rat and cat retinas, and quantitative BF MRI by continuous arterial spin labeling (ASL) (20). Multimodal MRI has also been applied to study retinal degeneration (17,20), diabetic retinopathy (21), and glaucoma (22,23) on rodent models.

Translation of retinal MRI applications from rodents to humans has two major challenges: (i) hardware that limits spatial resolution and signal-to-noise ratio on clinical MRI scanners and (ii) eye movement in awake humans. As a first step toward translation, we investigated the feasibility of multimodal retinal MRI on anesthetized/paralyzed large nonhuman primate (NHP) (baboon) using a standard clinical 3-Tesla MRI scanner. Baboon was chosen because the retina of baboon, compared with rodent, is evolutionarily closer to that of human and likely better recapitulates human retinal diseases. The size of baboon eye and the thickness of baboon retina are more similar to those of humans compared with rodents. Baboons have fovea in contrast to rodents and cats. Anesthesia and paralysis were used to exclude movement artifacts, such that we could focus on evaluating hardware feasibility, pulse sequence protocols, and parameters for high-resolution multimodal MRI of the retinas on a clinical scanner. These multimodal MRI protocols included anatomical MRI, basal BF MRI, BOLD fMRI of hyperoxic challenge, and BF fMRI of hypercapnic challenge. This study presents a novel approach to visualize anatomical, physiological (BOLD and BF), and fMRI of large NHP retinas on a clinical scanner, serving as a first step toward translation. Comparisons with published rodent and cat data are made.

MATERIALS AND METHODS

Animal Preparations

Seven normal baboons (*Papio hamadryas Anubis*; weighing 14–18 kg) were studied with approval of the Institutional Animal Care and Use Committee and in accordance with The Association for Research in Vision and Ophthalmology (ARVO) Statement for the Use of Animals in Ophthalmic and Vision Research. In group I, anatomical scans were performed on four baboons in five sessions with a total of eight trials. In group II, BOLD fMRI were performed on three baboons in four sessions with a total of 10 trials. In group III, BF measurements were obtained from three baboons in three sessions with a total of eight trials. Each session was performed on different day.

The baboon model, which offered high degree of stability, has been described previously (24). Briefly, anesthesia was initially inducted using ketamine (1.2 cc, i.m.), followed by oral intubation and cannulation of the right saphenous vein for fluid supplement and contrast agent administration. Animals were mechanically ventilated (Aestiva 5, Datex-Ohmeda, Madison, WI) at ~10 strokes/min and 120–180 mL/stroke. Anesthesia was maintained using 0.8–1.0% isoflurane in air. The animal was positioned supine in a custom-made animal holder and stabilized with ear bars, mouth bar, and padding

around the head. Rectal temperature was maintained within normal physiological ranges (37–38°C) using a custom-built feedback-regulated circulating warm-air blanket. End-tidal CO₂, O₂ saturation, heart rate, and respiration rate were monitored continuously using an MRI compatible physiological monitoring equipment (Precess, InVivo, Orlando, FL) and were maintained within normal physiological ranges. Vecuronium was administered immediately before placing the animal inside the scanner and was maintained throughout the entire MRI study (0.1 mg/kg initial dose, followed by 10% of initial dose every 45 min). At the end of the MRI experiments, neostigmine (0.5–2 mg, i.v.) and atropine (0.6–1.2 mg, i.v.) were administered to reverse paralysis. All animals recovered from anesthesia and paralysis.

In group I, to enhance the anatomical retinal vascular layers, Gadolinium Diethylenetriaminepenta acetic Acid (Gd-DTPA) (0.2–0.3 mmol/kg, Magnevist®, *N* = 2 of 5 baboons) was intravenously infused over a few minutes and MRI measurements were made before and immediately after Gd-DTPA injection. In group II, to modulate the BOLD MRI signals, subjects were ventilated with air (2 min), oxygen (3 min), and air (5 min) during MRI acquisition. In group III, to modulate the BF MRI signals, subjects were ventilated with air (3 min) and 5% CO₂ in air (4 min) during MRI acquisition. A break of 5–10 min was given between trials. Multiple trials were repeated on each imaging session.

To verify that BF contrast signals are genuine, BF MRI was also measured on an additional animal (*N* = 1) alive and postmortem in the same setting. This animal was scheduled for necropsy due to unrelated clinical reasons and was euthanized in the scanner.

MRI

MRI studies were performed on a 3-T Siemens TIM Trio (Siemens, Erlangen, Germany) using a body radiofrequency coil for transmission and a Siemens small receive-only surface coil (4 cm) for anatomical MRI and BOLD fMRI, and an eight-channel transmit/receive volume coil (human kneel coil, InVivo, Orlando, FL) for BF MRI and fMRI.

Anatomical MRI was acquired using fast low angle shot (FLASH) or balanced steady-state free precession (bSSFP) (25). The FLASH parameters were: repetition time (TR) = 50 ms, echo time = 3 ms, flip angle = 50°, a single slice thickness = 2 mm, readout bandwidth = 16 kHz, FOV = 29 × 29 mm², and matrix size = 290 × 145 (0.1 × 0.2 × 2.0 mm³ resolution). The higher in-plane resolution was placed perpendicular to the retina (anterior–posterior direction) to minimize partial volume effect (PVE). Precontrast and postcontrast enhanced images were acquired in time series for 15 min each. The bSSFP parameters were: TR = 12 ms, echo time = 3 ms, flip angle = 40°, slice thickness = 2 mm, readout bandwidth = 21 kHz, FOV = 50 × 50 mm², and matrix size = 500 × 250 (0.1 × 0.2 × 2.0 mm³ resolution). Precontrast and postcontrast enhanced images were acquired in time series for 6 min each.

BOLD MRI was acquired using a BOLD-sensitive pass-band bSSFP technique (26). The imaging parameters

were: TR = 8 ms, echo time = 4 ms, flip angle = 40°, a single slice thickness = 2 mm, readout bandwidth = 36 kHz, FOV = 50 × 50 mm², and matrix = 150 × 75 (0.3 × 0.6 × 2.0 mm³ resolution). A nonslice selective inversion recovery pulse was employed to suppress vitreous signal (inversion delay = 1800 ms). The temporal resolution per image was 4 s. Each stimulus trial took 10 min.

BF MRI was acquired using the pseudo-continuous ASL technique with a single-shot gradient echo-planar imaging. The imaging parameters were: TR = 3500 ms, echo time = 16 ms, labeling duration = 2.1 sec, labeling gradient of 0.6 G/cm, postlabeling delay = 700 ms, labeling offset = 60 mm, matrix = 64 × 64, FOV = 128 × 128 mm², and 12 contiguous slices with 2 mm slice thickness (2 × 2 × 2 mm³ resolution). Two of the eight trials were acquired with 4 mm slice thickness. Each stimulus trial took 7 min. Specific absorption rate was not an issue for the pseudo-continuous ASL protocol as the protocol was essentially identical to typical human brain pseudo-continuous ASL BF measurements and was verified by the scanner safety monitor.

Data Analysis

Image analysis was performed using Matlab (MathWorks Inc, Natick, MA) and FMRIB Software Library (FSL) (FMRIB Centre, Oxford, UK). All images were acquired in time series and coregistered using custom-written algorithm in Matlab. The retina was automatically detected using an edge-detection technique as previously described (17). Radial projections perpendicular to the vitreous boundary were obtained with three or four times the sampling density of the original image, and projection profiles at different time points were then coregistered to the averaged profile by minimizing the root-mean-square distances. Time-series movies of MR images were carefully evaluated to verify the absence of gross motion or drift before further analysis.

To quantitatively determine laminar thickness, the edge-detection technique described above was employed and the projection profiles were averaged along the length of the retina. Band thicknesses were determined from the averaged projection profile using the “half height” method as commonly used to measure vessel diameters in optical imaging studies.

BOLD fMRI activation maps were generated using FSL. A cross correlation analysis was performed by matching the fMRI signal time courses to the stimulus paradigm with a background signal intensity threshold applied before fMRI analysis to exclude low intensity pixels (such as noisy background and the suppressed vitreous). A cluster analysis with cluster size $P < 0.05$ was further imposed to threshold the cross correlation map. Time courses had band-pass temporal smoothing (range of 0.002–0.1Hz). Quantitative analysis of fMRI percent changes used a region of interest (ROI) analysis to avoid correlation bias. Percent changes were tabulated for 90% of maximal signal changes. Regional variations of the fMRI responses along the length of the retina were also evaluated.

BF in mL/100 g/min was calculated pixel-by-pixel using (24), $BF = \frac{\lambda \Delta M}{2\alpha M_0 T_{1a} (e^{-w/T_{1a}} - e^{-(\tau+w)/T_{1a}})}$, where α is the labeling efficiency, λ is the water brain-blood partition

coefficient, T_{1a} is the longitudinal relaxation time of arterial blood, w is the postlabeling delay, and τ is the labeling duration. λ of 0.9, α of 0.8, τ of 2.1 sec, and T_{1a} of 1.66 s at 3 T were used. BF changes due to hypercapnia in the retina were also analyzed as described above for the BOLD data. For comparison, basal BF and hypercapnia-induced BF changes for gray matter and white matter from the brain were also tabulated. Gray matter and white matter of the brain were segmented based on T_1 -weighted anatomical MRI as described previously (24).

All statistical tests employed t -test unless otherwise specified. $P < 0.05$ was taken to be statistically significant.

Histology

Four eyes from two additional female baboons (both 19 years old; weighing 14 and 18.5 kg, respectively) were enucleated and immersion fixed in 10% neutral buffered formalin immediately after postmortem. These eyes were obtained from necropsy, different from those of the survival MRI studies. Eyes were paraffin embedded and sectioned at 12 μ m and stained with haematoxylin eosin (H&E) stain. Each histological section was digitally photographed within 2–5 days postmortem and laminar thicknesses were measured at 100X.

RESULTS

Anatomical MRI

The diameter of the baboon eye was 21.8 ± 0.4 mm (mean \pm standard deviation [SD]; four baboons) in the anterior–posterior direction as measured by MRI. Assuming a sphere, PVE due to the curvature of the retina was 15.2% of the total retinal thickness for a central imaging slice of 2 mm. Because the retina is relatively flat at the posterior pole, where the fovea and optic nerve head (ONH) are located, this estimate likely reflected the upper limit. Figure 1A shows a representative T_1 -weighted gradient-echo (FLASH) image of a normal retina revealed three distinct “layers” as indicated by the alternating bright, dark, and bright bands. The adjacent vitreous and sclera appeared relatively hypointense because of the long T_1 of the vitreous, and the short effective transverse relaxation time (T_2^*) of the sclera. The optic nerve, rectus muscles, lens, anterior chambers, iris, and ciliary bodies among others were also clearly delineated. Administration of the intravenous contrast agent Gd-DTPA markedly enhanced the inner and outer bands, but not in the middle bands, lens, or vitreous. In addition, the outer band was more enhanced than the inner band (Fig. 1B). The subtraction of precontrast from postcontrast images demonstrated the localization of Gd-DTPA impermeable vasculature on either side of the retina (Fig. 1C). Note that the extraocular tissue and the anterior chamber were also enhanced by Gd-DTPA.

To improve temporal resolution and to corroborate laminar resolution, we explored bSSFP acquisition. Figure 2 shows the bSSFP images before and after Gd-DTPA administration. Similar alternating bright, dark, and bright bands were observed before Gd-DTPA. The two bounding layers were enhanced after Gd-DTPA. The total scan time was 6 min compared with the 15-min FLASH

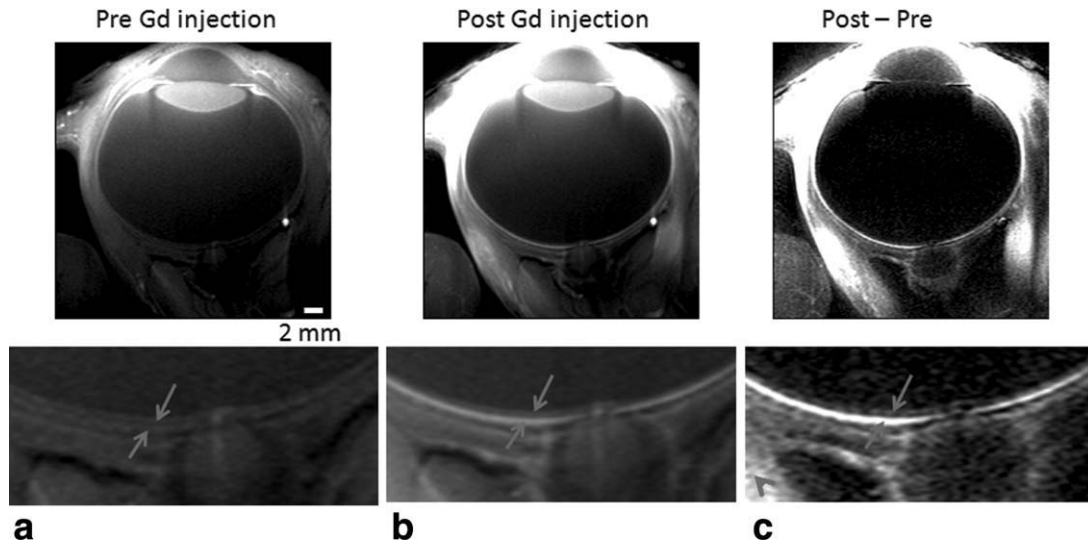


FIG. 1. Anatomical MRI (FLASH) at $0.1 \times 0.2 \times 2 \text{ mm}^3$ from a normal baboon (a) before and (b) after Gd-DTPA administration and (c) the subtracted image. Three distinct “layers” of alternating bright, dark, and bright bands are evident. The two (blue) arrows in the expanded views indicate the inner and outer bands of the retina corresponding to the two vascular layers, bounding the retina. The (red) arrowhead indicates signal enhancement of extra-ocular tissues.

acquisition. Signal-to-noise ratio was apparently improved as well, although quantitative comparison was not performed.

Retinal thickness was calculated using edge-detection technique. The group-averaged total retinal thickness including the CH were plotted along the length of the retina (Fig. 3A). The retina including the CH was thickest around the fovea and the ONH, and the thickness tapered off toward the distal edges of the retina. Foveal pit and the pit of the ONH were not clearly resolved, likely due to the thick imaging slice and PVE. The thicknesses for the three “layers” were analyzed for an ROI including the fovea as shown in the inset of Fig. 3B. The group-averaged thicknesses were 218 ± 42 , 182 ± 40 , and $217 \pm 59 \mu\text{m}$ by MRI (mean \pm SD, $N = 8$ trials), for the inner, middle, and outer MRI “layers”, respectively. The total retinal thickness including the CH was $617 \pm 101 \mu\text{m}$ from the same ROI. The group-averaged inner-to-outer peak distance was $375 \pm 91 \mu\text{m}$.

A histological section depicting different cell layers and a distinct choroidal vascular layer is shown in Fig. 4. The nerve fiber layer (NFL), ganglion cell layer (GCL), inner plexiform layer (IPL), inner nuclear layer (INL), outer plexiform layer (OPL), outer nuclear layer (ONL), inner segment,

outer segment, and CH were clearly identified. Comparative analysis between MRI and histology yielded the following layer assignments. Gd-DTPA enhanced the inner band of MRI, which was assigned to include the GCL and inner nuclear layer with embedded retinal vasculature. The middle band, which appeared relatively hypointense on anatomical imaging, was not enhanced by Gd-DTPA and was thus assigned to include the avascular ONL and the photoreceptor segments. Gd-DTPA enhanced the outer band, which was assigned as the CH. The corresponding histological inner, middle, and outer band thicknesses for the MRI bands were, respectively, 122 ± 7 (NFL, GCL, IPL, and OPL), 113 ± 8 (ONL, inner segment, and outer segment), and $91 \pm 3 \mu\text{m}$ (CH), with a total thickness of $326 \pm 10 \mu\text{m}$ (mean \pm SD, $N = 4$ eyes), including the CH.

BOLD MRI

Dynamic BOLD fMRI was used to probe the responses to oxygen inhalation relative to air (Fig. 5). BOLD fMRI responses were detected to be highly localized to the retina. The group-averaged time course from the posterior retina ROI showed increased BOLD signals during oxygen inhalation compared with air, with a mean BOLD

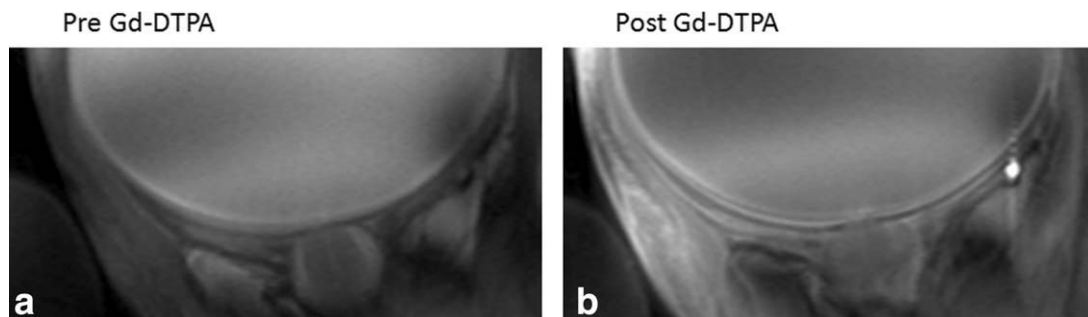


FIG. 2. Anatomical MRI (bSSFP) at $0.1 \times 0.2 \times 2 \text{ mm}^3$ from a normal baboon (a) before and (b) after Gd-DTPA administration. Three distinct “layers” (arrows) of alternating bright, dark, and bright bands are evident.

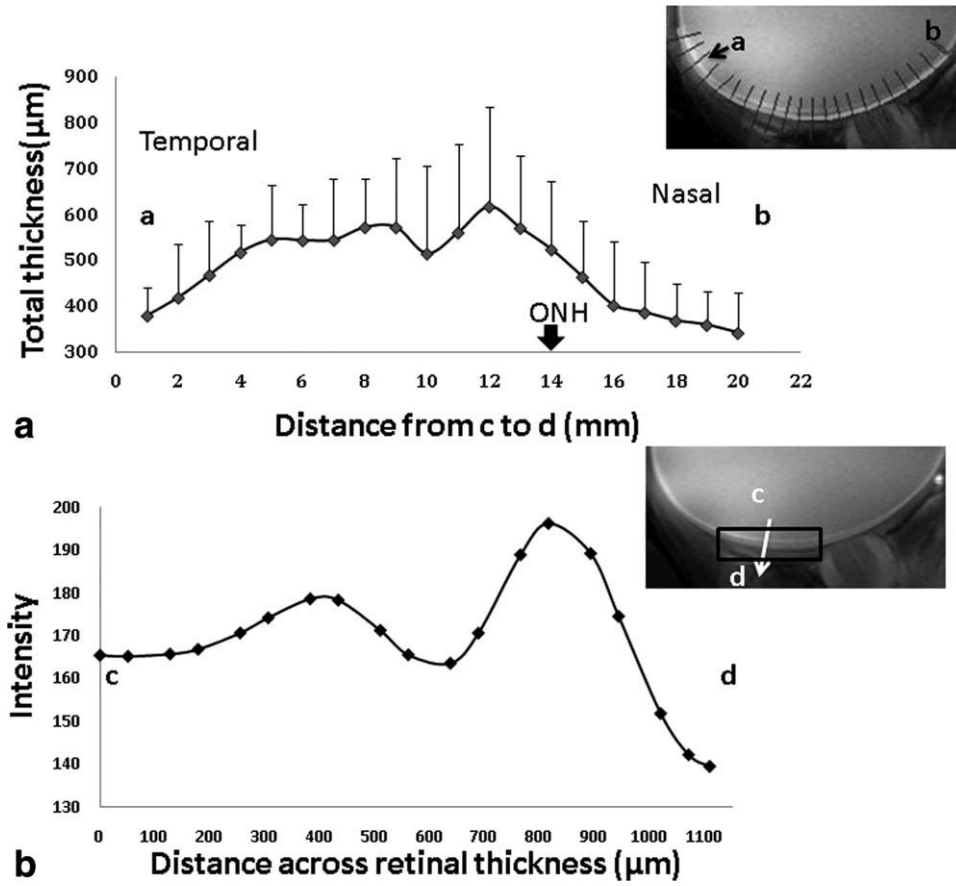


FIG. 3. **a**: Retinal thickness as a function of distance from the optic nerve head (ONH), obtained from point *a* to *b* (mean \pm SD, $N = 8$ trials, error bars are SDs). Inset: the blue radial lines across the retinal thickness show how the profiles are obtained by the automated program. **b**: Projection profile across the retinal thickness, obtained from point *c* to *d*. The retina was segmented using edge-detection technique. Projection profiles across the retinal thickness were summed along the length of the retina over the ROI shown. Inset: ROI used for group-averaged thicknesses reported in text.

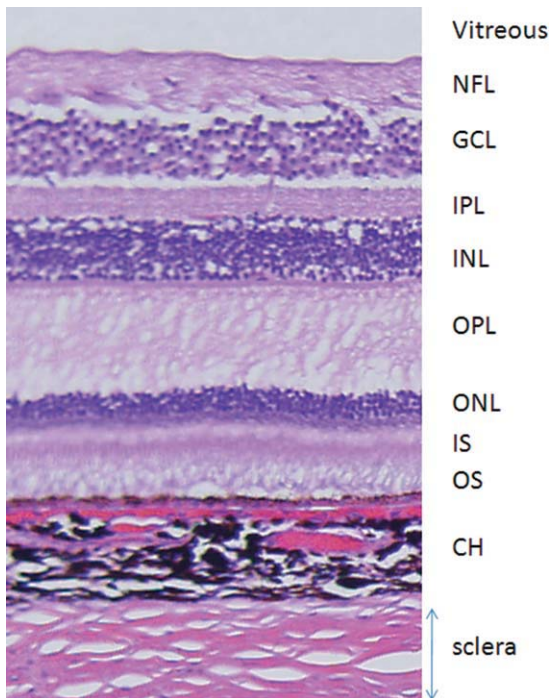


FIG. 4. A H&E histological slide of baboon retina. NFL: nerve fiber layer, GCL: ganglion cell layer, IPL: inner plexiform layer, INL: inner nuclear layer, OPL: outer plexiform layer, ONL: outer nuclear layer, IS: inner segment, OS: outer segment, and CH: choroid.

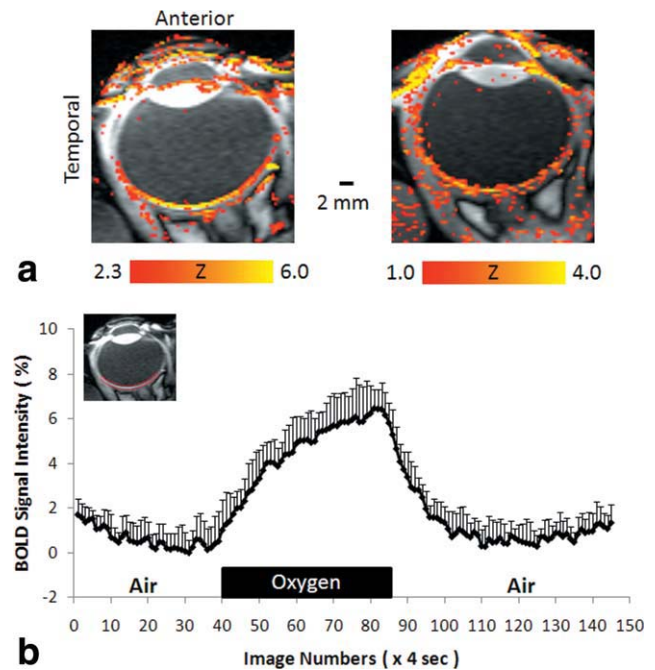


FIG. 5. **a**: BOLD fMRI at $0.3 \times 0.6 \times 2 \text{ mm}^3$ of oxygen vs. air inhalation from two subjects, and **(b)** the group-averaged time course of oxygen versus air inhalation. Inset image: ROI used to obtain the group-averaged time course. Error bars are SDs across trials. Note that scattered activations in the ciliary bodies and extraocular tissue are also expected as oxygen inhalation causes global BOLD increases.

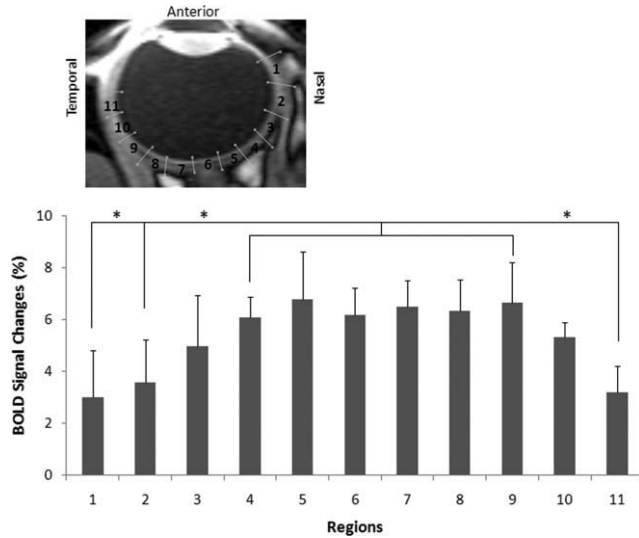


FIG. 6. Spatial dependence of BOLD fMRI percent changes due to oxygen inhalation (mean \pm SD, $N = 10$ trials). There was no significant difference between any two regions from 3 to 10 ($P > 0.05$ by Tukey Honestly Significant Difference). There were significant differences between regions 1, 2, and 11 versus any region from 4 to 9 ($P < 0.05$ by Tukey Honestly Significant Difference). * indicates statistical significance.

increase of $6.5 \pm 1.4\%$ (mean \pm SD, $N = 10$ trials). BOLD responses were also detected globally in the rectus muscles and ciliary bodies but were largely absent from the vitreous and lens as expected. The group-averaged BOLD percent changes are plotted along the length of the retina in Fig. 6. BOLD percent changes showed spatial dependence, with the responses being significantly stronger around the fovea and the ONH than the distal edges of the retina ($P < 0.05$ by Tukey Honestly Significant Difference).

BF MRI

Figure 7A shows the BF images obtained using BF MRI from one representative animal. BF contrast was reliably detected. The highest BF was at the posterior pole and dropped off distally. To verify, BF contrast signals are genuine; BF was also measured in alive and postmortem animal ($N = 1$) in the same setting where the animal was euthanized in the magnet for unrelated clinical reasons. The results showed no significant BF contrasts in the postmortem retina and brain (data not shown), indicating no significant unwanted magnetization-transfer effect.

Group-averaged basal BF and hypercapnia-induced BF changes of the retina, white matter, and gray matter of the brain were analyzed from the same animals (Fig. 7B). Basal BF from the posterior retina ROI was 83 ± 30 mL/100 g/min (mean \pm SD, $N = 8$ trials). Hypercapnia increased BF by $25 \pm 9\%$ in the retina. By comparison, basal BF values of the gray matter and white matter were 60 ± 12 and 24 ± 3 mL/100 g/min, respectively. Hypercapnia increased BF by $74 \pm 13\%$ and $85 \pm 23\%$ in the gray matter and white matter, respectively. The basal BF of the retina and gray matter were significantly higher than that of the white matter ($P < 0.01$). Although the BF of the

retina was higher than that of gray matter, no significant difference was found between them for the given sample size ($P > 0.05$). Hypercapnic-induced BF percent changes were higher in the brain than in the retina ($P < 0.01$).

DISCUSSION

This study demonstrates hardware feasibility of high-resolution multimodal MRI of the retinas of large NHPs using a clinical 3T scanner. Anatomical MRI reveals multiple tissue and vascular “layers” in the retina. Gd-DTPA enhanced MRI corroborates layer assignments. Basal BF, hyperoxia-induced BOLD changes, and hypercapnia-induced BF changes in the retina are reliably detected. Although spatial resolution needs improvement and will be the target of future investigations, this report provides encouraging data to explore retinal MRI in large NHPs and human.

The advantages of MRI include depth resolution, images unhindered by media opacity, and a large FOV; whereas the disadvantages of MRI include poorer spatio-temporal resolution and high cost, compared with optical imaging techniques. MRI could provide valuable, clinically relevant anatomical, physiological, and functional data, which may be helpful for early detection and staging of retinal diseases, as well demonstrated in many neurological disorders. This approach also has the potential to complement existing retinal imaging techniques.

Potential Issues

High-resolution MRI of the NHP retina may be susceptible to hardware and eye drift artifacts because high-resolution imaging pulse sequences are more demanding on

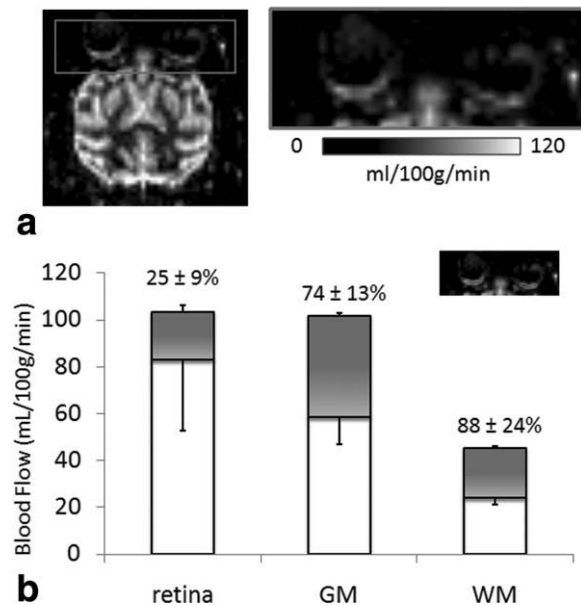


FIG. 7. **a**: Basal BF image of a baboon retina at $2 \times 2 \times 2$ mm³. **b**: Group-averaged basal BF and hypercapnia-induced BF changes (shaded regions) of the retina, gray matter (GM), and white matter (WM) of the brain (mean \pm SD, $N = 8$ trials). Inset: typical ROIs of the posterior retina used for group-averaged analysis.

the magnetic field gradient, which can lead to temperature-induced frequency and signal drift. We confirmed on phantoms that our imaging protocols with identical parameters did not have significant hardware-related drift over half an hour of data acquisition (data not shown). The eye could drift significantly despite the animal being under anesthesia (27). To ensure the absence of movement artifacts and drifts, time-loop movies of the raw data and center-of-mass time courses were evaluated. Signal time courses were also evaluated to ensure no sudden jumps or significant drift. These precautions were necessary because signal contamination from either side of the retina due to misregistration would markedly affect signal intensities.

PVE due to the thin retina could be significant because the thin retina is bounded by the vitreous and the sclera, which have very different signal intensities from that of the retina. Although vitreous signals were suppressed using short TR in anatomical MRI and inversion pulse in BOLD MRI, PVE could affect retinal thickness, basal BF, BOLD and BF percent change measurements. Future studies will need to improve spatial resolution and sensitivity to improve laminar thickness quantification, and to differentiate BOLD and BF MRI signal changes between the retinal and choroidal vasculatures.

Absolute quantification of BF is generally difficult. The pseudo-continuous ASL MRI technique to measure BF of the retina has the following limitations. BF calculation used the blood-tissue partition coefficient (λ) of the brain (28) because blood-tissue partition coefficient in the retina has not been measured. This assumption is reasonable because the retina is part of the central nervous system. In addition, brain T_1 was used in the BF calculation. Retina T_1 has been reported to be similar to brain T_1 in animals (29). BF MRI of the brain has been cross-validated with positron emission tomography and autoradiographic techniques. Ultimately, ASL MRI of the retina needs to be cross validated with microsphere or iodoantipyrine technique in animal models. Improving accuracy of quantitative BF MRI remains an active area of research.

Anatomical MRI

Three distinct “layers” of alternating bright, dark, and bright bands were resolved. The vitreous and sclera set the boundaries of the retina. The retinal vessels consist of nonfenestrated capillaries, forming the blood-retinal barriers, which are impervious to many tracers, including Gd-DTPA. In the choroidal circulation, tight-junctions between retinal epithelial cells prevent passages of large molecules (including Gd-DTPA) from the choriocapillaris (30). Thus, Gd-DTPA selectively enhances signal in the blood vessels, providing valuable contrast. Indeed, subtraction of postcontrast and precontrast images from the Gd-DTPA experiments showed marked signal enhancement on either side of the retina, with the outer band being more enhanced than the inner band. The contrast-enhanced imaging results indicated that: (i) there are two vascular layers located at either end of the retina with the middle of the retina being avascular, as expected (17,18,31). (ii) The choroidal vasculature has

markedly higher BF and blood volume than the retinal vasculature, consistent with established differences in BF between the two vasculatures (2,17,18). The Gd-DTPA enhancement and laminar assignments herein are in good agreement with previous MRI studies in rats (17) and cats (18).

MRI-derived total retinal thickness including the CH was $617 \pm 101 \mu\text{m}$ at the posterior retina, which was thicker than that by histology of $326 \pm 10 \mu\text{m}$ ($P < 0.05$). If PVE of 15% due to curvature was applied (17), the MRI-derived total retinal thickness including the CH would be $537 \mu\text{m}$, which was still significantly thicker than that by histology. Discrepancy between MRI and histological thicknesses could arise from collapse of choroidal vessels after removal of orbits from the systemic circulation, histological shrinkage, differences in retinal regions analyzed, different animals being used for MRI and histology, and/or PVE due to MRI spatial resolution. To our knowledge, there are no published baboon retinal thicknesses with which to compare. By comparison with the rat retina, the inner, middle, and outer band thicknesses of adult Sprague–Dawley rat retinas were, respectively, 101 ± 17 , 79 ± 11 , and $86 \pm 10 \mu\text{m}$ by MRI ($n = 24$, total thickness $267 \pm 31 \mu\text{m}$), which were also thicker than those by histology, i.e., 92 ± 9 , 77 ± 9 , and $37 \pm 8 \mu\text{m}$ (SD, $n = 9$, total thickness = $205 \pm 11 \mu\text{m}$) (17). By appearance of histology, the baboon retina was substantially different from rat retina (32). For example, baboon NFL and OPL were comparatively thicker, whereas IPL and ONL were comparatively thinner, relative to the overall thicknesses.

There was a strong spatial dependence in the total thickness of the retina including the CH along the length of the retina (Fig. 3A). The retina/CH complex was thicker immediate adjacent to the ONH, on the side of the fovea based on optical coherence tomography data (33). In around the expected region of the fovea, the retina/CH complex was thinner slightly compared with its surrounding regions on either side, likely because the retinal thickness reach a minimum at the fovea (34). The total thickness dropped off markedly away from the macular area as expected (33,35).

BOLD MRI

Oxygen inhalation relative to air is expected to increase arteriole, capillary, and venous oxygen saturation and thus is expected to increase BOLD signal, as well demonstrated in the brain (36). Oxygen inhalation has been reported to increase BOLD signals in the gray matter of the rhesus monkey brain by 2.4% at 3T (37). Because choroidal BF is much higher than retinal BF, the observed BOLD signal is likely predominant from choroidal vasculature. The arteriovenous oxygen difference in the CH (2) is small compared with that of the brain. Thus, one might expect a small hyperoxia-induced BOLD increase. In contrast, the group-averaged BOLD increase in the retina/CH complex during oxygen challenge was $6.5 \pm 1.4\%$, generally larger than those of the brain. This is likely because the CH has a high vascular density, and thus the larger percent changes. In addition, it is worth pointing out that hyperoxia markedly

decreases retinal BF (by 60% relative to air inhalation) (38), but has no effect on choroidal vessels (39). By comparison, hyperoxia decreases brain BF by $\sim 10\%$ (40). Such vasoconstriction would tend to counteract the BOLD signal increase from elevated oxygen tension by hyperoxia per se. The net effect observed in our study is a positive BOLD increase, suggesting that the increased oxygen delivery per se from oxygen inhalation dominates. The results herein are in good agreement with previous BOLD fMRI study of oxygen challenge in the rat retina, which also detected positive BOLD signal changes (17). Further exploration of laminar-specific BOLD and BF measurements would help to detect these unique vascular responses in the retina.

There was a strong spatial dependence in the BOLD responses along the length of the baboon retina (Fig. 6). The responses were the strongest around the fovea and the ONH and dropped off distally. This appeared consistent with similar profiles in layer thickness (Fig. 3A) and BF values (Fig. 7).

Blood Flow

Under normal physiological conditions, BF is intricately coupled to basal metabolism and function, as well demonstrated in the brain. Basal BF of the total retina, including the CH was 83 ± 30 mL/100 g/min in anesthetized baboon. Basal BF of the rat retina has been reported to be 630 ± 100 mL/100 g/min under 1% isoflurane also using ASL MRI (20).

The anesthetized baboon brain gray matter BF was 60 ± 12 mL/100 g/min obtained in the same animals, consistent with previous brain BF data in baboon (24). By comparison, BF of the entire rat brain was ~ 100 mL/100 g/min under similar experimental conditions (41,42). The BF retina:brain ratio was 6.3:1 in rat and 1.3:1 in baboon. This difference could be because of differences in spatial resolutions and/or species.

Hypercapnic inhalation is expected to increase BF, as well demonstrated in the brain (36). In the baboon brain, BF in the gray matter increased $74 \pm 13\%$. In the rat brain, hypercapnic (5% CO₂ in air) inhalation increased cerebral BF varied over a wide range, but has been reported to increase $\sim 50\%$ (42) in anesthetized rats. Similar hypercapnia-induced changes in cerebral BF in humans under different anesthetics have also been reported in the literatures. Hypercapnia-induced BF increase in the baboon retina ($25 \pm 9\%$) appears to be smaller than in the brain, consistent with $16 \pm 6\%$ increase in rat retina (43). The high basal choroidal BF could reduce head room for additional vasodilation (42).

Species Differences

Retinal thickness, BF value, and fMRI percent changes of baboon retinas differed from rat (17) and cat (18) data. Baboon retinal thickness including the CH was about double that of rat or cat. The baboon retina showed heterogeneity, revealing indentation of the fovea and ONH (Fig. 3A) in contrast to rat data, which was relatively uniform by MRI (17). Retinal thickness in baboon showed a rapid drop off as a function of distance away

from the ONH, in contrast to rat data which was relatively uniform (17). There were also the marked differences in histological appearances. For example, with respect to the overall thicknesses, the baboon NFL and OPL are thicker; whereas IPL and ONL are thinner compared with the rat retina. Baboon, in contrast to cat, does not have a tapetum (18). Baboon has a fovea, whereas neither rat nor cat has a fovea.

BF of the baboon retina was also lower than that in rat retina, consistent with baboon brain BF also being lower than rat brain BF. Larger animals generally have lower basal BF (which reflects lower basal metabolic rate) than smaller animals. Moreover, BF of the retina in baboon showed a rapid drop off as a function of distance from the ONH, in contrast to rat BF data which appeared more uniform (43). Cognizant of more PVE in the baboon retinal data, these comparisons suggest there are species differences and warrant further investigations.

CONCLUSION

This study reports a proof-of-concept that anatomical MRI, hyperoxia-induced BOLD fMRI changes, quantitative basal BF, and hypercapnia-induced BF fMRI in the retina of anesthetized baboon can be imaged using a clinical 3 Tesla scanner. Comparison with rodent and cat data revealed some species differences in retina thickness, BF value, and fMRI responses. These findings offer encouraging data to explore human applications. Indeed, retinal MRI in humans has recently been reported (44–46). Translating high-resolution anatomical, physiological (BF and oxygenation tension), and fMRI to image the unanesthetized human retina could have important applications. Irrespective of whether these approaches can be translated to humans or clinics, they can be used to study retinal diseases and to test novel therapeutic strategies in the retinas of large NHPs, which likely better model human retinal diseases compared with rodents.

ACKNOWLEDGMENTS

The authors Yi Zhang and Hsiao-Ying Wey contributed equally to this work.

REFERENCES

- Wassle H, Boycott BB. Functional architecture of the mammalian retina. *Physiol Rev* 1991;1:447–480.
- Bill A. Circulation in the eye. In: Renkin EM, Michel CC, editors. *Handbook of physiology: The cardiovascular system IV*. Bethesda, MD: American Physiological Society; 1984:1001–1034.
- Pemp B, Schmetterer L. Ocular blood flow in diabetes and age-related macular degeneration. *Can J Ophthalmol* 2008;43:295–301.
- Pourmaras CJ, Rungger-Brandle E, Riva CE, Hardarson SH, Stefansson E. Regulation of retinal blood flow in health and disease. *Prog Retin Eye Res* 2008;27:284–330.
- Fujimoto JG, Brezinski ME, Tearney GJ, Boppart SA, Bouma B, Hee MR, Southern JF, Swanson EA. Optical biopsy and imaging using optical coherence tomography. *Nat Med* 1995;1:970–972.
- Shonart RD, Richmond KN, Johnson PC. Phosphorescence quenching and the microcirculation: an automated, multipoint oxygen tension measuring instrument. *Rev Sci Instrum* 1995;66:5075–5084.
- Grinvald A, Bonhoeffer T, Vanzetta I, Pollack A, Aloni E, Ofri R, Nelson D. High-resolution functional optical imaging: from the neocortex to the eye. *Ophthalmol Clin North Am* 2004;17:53–67.
- Preussner PR, Richard G, Darrelmann O, Weber J, Kreissig I. Quantitative measurement of retinal blood flow in human beings by

- application of digital image-processing methods to television fluorescein angiograms. *Graefes Arch Clin Exp Ophthalmol* 1983;221:110–112.
9. Guyer DR, Yannuzzi LA, Slakter JS, Sorenson JA, Orlock S. The status of indocyanine-green videoangiography. *Cur Opin Ophthalmol* 1993;4:3–6.
 10. Formaz F, Riva CE, Geiser M. Diffuse luminance flicker increases retinal vessel diameter in human. *Curr Eye Res* 1997;16:1252–1257.
 11. Cheng H, Duong TQ. Simplified laser-speckle-imaging analysis method and its application to retinal blood flow imaging. *Opt Lett* 2007;32:2188–2190.
 12. Kim D-S, Duong TQ, Kim S-G. High-resolution mapping of iso-orientation columns by fMRI. *Nature Neurosci* 2000;3:164–169.
 13. Duong TQ, Kim D-S, Ugurbil K, Kim S-G. Localized blood flow response at sub-millimeter columnar resolution. *Proc Natl Acad Sci USA* 2001;98:10904–10909.
 14. Cheng K, Waggoner RA, Tanaka K. Human ocular dominance columns as revealed by high-field functional magnetic resonance imaging. *Neuron* 2001;32:359–397.
 15. Silva AC, Koretsky AP. Laminar specificity of functional MRI onset times during somatosensory stimulation in rat. *Proc Natl Acad Sci USA* 2002;99:15182–15187.
 16. Goense JB, Logothetis NK. Laminar specificity in monkey V1 using high-resolution SE-fMRI. *Magn Reson Imaging* 2006;24:381–392.
 17. Cheng H, Nair G, Walker TA, Kim MK, Pardue MT, Thule PM, Olson DE, Duong TQ. Structural and functional MRI reveals multiple retinal layers. *Proc Natl Acad Sci USA* 2006;103:17525–17530.
 18. Shen Q, Cheng H, Pardue MT, Chang TF, Nair G, Vo VT, Shonat RD, Duong TQ. Magnetic resonance imaging of tissue and vascular layers in the cat retina. *J Magn Reson Imaging* 2006;23:465–472.
 19. Duong TQ, Ngan S-C, Ugurbil K, Kim S-G. Functional magnetic resonance imaging of the retina. *Invest Ophthalmol Vis Sci* 2002;43:1176–1181.
 20. Li Y, Cheng H, Shen Q, Kim M, Thule PM, Olson DE, Pardue MT, Duong TQ. Blood-flow magnetic resonance imaging of retinal degeneration. *Invest Ophthalmol Vis Sci* 2009;50:1824–1830.
 21. Berkowitz BA, Roberts R, Luan H, Peysakhov J, Mao X, Thomas KA. Dynamic contrast-enhanced MRI measurements of passive permeability through blood retinal barrier in diabetic rats. *Invest Ophthalmol Vis Sci* 2004;45:2391–2398.
 22. Calkins DJ, Horner PJ, Roberts R, Gadianu M, Berkowitz BA. Manganese-enhanced MRI of the DBA/2J mouse model of hereditary glaucoma. *Invest Ophthalmol Vis Sci* 2008;49:5083–5088.
 23. Chan KC, Fu QL, Hui ES, So KF, Wu EX. Evaluation of the retina and optic nerve in a rat model of chronic glaucoma using in vivo manganese-enhanced magnetic resonance imaging. *Neuroimage* 2008;40:1166–1174.
 24. Wey HY, Wang DJ, Duong TQ. Baseline CBF, and BOLD, CBF, and CMRO2 fMRI of visual and vibrotactile stimulations in baboons. *J Cereb Blood Flow Metab* 2010;31:715–724.
 25. Scheffler K, Lehnardt S. Principles and applications of balanced SSFP techniques. *Eur Radiol* 2003;13:2409–2418.
 26. Miller KL, Smith SM, Jezzard P, Wiggins GC, Wiggins CJ. Signal and noise characteristics of SSFP fMRI: a comparison with GRE at multiple field strengths. *Neuroimage* 2007;37:1227–1236.
 27. Duong TQ, Muir ER. Magnetic resonance imaging of the retina. *Jpn J Ophthalmol* 2009;53:352–367.
 28. Herscovitch P, Raichle ME. What is the correct value for the brain-blood partition coefficient for water? *J Cereb Blood Flow Metab* 1985;5:65–69.
 29. Nair G, Shen Q, Duong TQ. Relaxation time constants and apparent diffusion coefficients of rat retina at 7 Tesla. *Int J Imag Syst Tech* 2010;20:126–130.
 30. Vinores SA. Assessment of blood-retinal barrier integrity. *Histol Histopathol* 1995;10:141–154.
 31. Harris A, Kagemann L, Cioffi GA. Assessment of human ocular hemodynamics. *Survey of Ophthalmol* 1998;42:509–533.
 32. Duong TQ, Pardue MT, Thule PM, Olson DE, Cheng H, Nair G, Li Y, Kim M, Zhang X, Shen Q. Layer-specific anatomical, physiological and functional MRI of the retina. *NMR Biomed* 2008;21:978–996.
 33. Cheng S, Lam C, Yap M. Retinal thickness in myopic and non myopic eyes. *Ophthalmic Physiol Opt* 2010;30:776–784.
 34. Sanchez-Tocino H, Alvarez-Vidal A, Maldonado M, Moreno-Montanes J, Garcia-Layana A. Retinal thickness study with optical coherence tomography in patients with diabetes. *Invest Ophthalmol Vis Sci* 2002;43:1588–1594.
 35. Manjunath V, Taha M, Fujimoto JG, Duker JS. Choroidal thickness in normal eyes measured using Cirrus HD optical coherence tomography. *Am J Ophthalmol* 2010;150:325–329 e321.
 36. Raichle ME. Circulatory and metabolic correlates of brain function in normal humans. In: Plum F, editor. *Handbook of physiology—the nervous system V: higher functions of the brain*. Bethesda, MD: American Physiological Society; 1987. pp 643–674.
 37. Zhang X, Nagaoka T, Auerbach EJ, Champion R, Zhou L, Hu X, Duong TQ. Quantitative basal CBF and CBF fMRI of rhesus monkeys using three-coil continuous arterial spin labeling. *Neuroimage* 2007;34:1074–1083.
 38. Riva CE, Grunwald JE, Singclair SH. Laser Doppler velocimetry study of the effect of pure oxygen breathing on retinal blood flow. *Invest Ophthalmol Vis Sci* 1983;24:47–51.
 39. Geiser MH, Riva CE, GDorner GT, Diermann U, Luksch A, Schmetterer L. Response of choroidal blood flow in the foveal region to peroxia and hyperoxia-hypercapnia. *Current Eye Res* 2000;21:669–676.
 40. Kety SS, Schmidt CF. The effects of altered arterial tensions of carbon dioxide and oxygen on cerebral blood flow and cerebral oxygen consumption of normal young men. *J Clin Invest* 1948;27:484–491.
 41. Sicard K, Shen Q, Brevard ME, Sullivan R, Ferris CF, King JA, Duong TQ. Regional cerebral blood flow and BOLD responses in conscious and anesthetized rats under basal and hypercapnic conditions: implications for functional MRI studies. *J Cereb Blood Flow Metab* 2003;23:472–481.
 42. Sicard KM, Duong TQ. Effects of hypoxia, hyperoxia and hypercapnia on baseline and stimulus-evoked BOLD, CBF and CMRO2 in spontaneously breathing animals. *Neuroimage* 2005;25:850–858.
 43. Li Y, Cheng H, Duong TQ. Blood-flow magnetic resonance imaging of the retina. *Neuroimage* 2008;39:1744–1751.
 44. Zhang Y, Peng Q, Kiel JW, Rosende CA, Duong TQ. Magnetic resonance imaging of vascular oxygenation changes during hyperoxia and carbogen challenges in the human retina. *Invest Ophthalmol Vis Sci* 2010;52:286–291.
 45. Peng Q, Zhang Y, Oscar San Emeterio Nateras O, van Osch MJP, Duong TQ. Magnetic resonance imaging of blood flow of the human retina. *Magn Reson Med* 2010, in press.
 46. Maleki N, Dai W, Alsop DC. Blood flow quantification of the human retina with MRI. *NMR Biomed* 2010, in press.